Nano Research 2014, 7(7): 1027–1042
DOI 10.1007/s12274-014-0466-3
Research Article

ISSN 1998-0124
CN 11-5974/O4

Green and low temperature synthesis of nanocrystalline transition metal ferrites by simple wet chemistry routes

Stefano Diodati[1], Luciano Pandolfo[2], Andrea Caneschi[3], Stefano Gialanella[4], and Silvia Gross[1,2] (✉)

[1] *Istituto per l'Energetica e le Interfasi, IENI-CNR and INSTM, UdR di Padova, via Marzolo, 1, I-35131, Padova, Italy*
[2] *Dipartimento di Scienze Chimiche, Università degli Studi di Padova, via Marzolo, 1, I-35131, Padova, Italy*
[3] *Laboratory of Molecular Magnetism, LAMM Dipartimento di Chimica e UdR INSTM di Firenze, Polo Scientifico, Via della Lastruccia, 3, 50019, Sesto Fiorentino (FI), Italy*
[4] *Dipartimento di Ingegneria Industriale, Università degli Studi di Trento, via Mesiano 77, I-38123, Trento, Italy*

Received: 9 January 2014
Revised: 27 March 2014
Accepted: 31 March 2014

KEYWORDS
ferrites,
hydrothermal,
low temperature,
wet chemistry,
green

ABSTRACT

Crystalline and nanostructured cobalt ($CoFe_2O_4$), nickel ($NiFe_2O_4$), zinc ($ZnFe_2O_4$) and manganese ($MnFe_2O_4$) spinel ferrites are synthesized with high yields, crystallinity and purity through an easy, quick, reproducible and low-temperature hydrothermal assisted route starting from an aqueous suspension of coprecipitated metal oxalates. The use of water as a reaction medium is a further advantage of the chosen protocol. Additionally, the zinc spinel is also prepared through an alternative route combining coprecipitation of oxalates from an aqueous solution with thermal decomposition under reflux conditions. The nanocrystalline powders are obtained as a pure crystalline phase already at the extremely low temperature of 75 °C and no further thermal treatment is needed. The structure and microstructure of the prepared materials is investigated by means of X-ray powder diffraction (XRPD), while X-ray photoelectron spectroscopy (XPS) and inductively coupled plasma–atomic emission spectroscopy (ICP–AES) analyses are used to gain information about the surface and bulk composition of the samples, respectively, confirming the expected stoichiometry. To investigate the effect of the synthesis protocol on the morphology of the obtained ferrites, transmission electron microscopy (TEM) observations are performed on selected samples. The magnetic properties of the cobalt and manganese spinels are also investigated using a superconducting quantum device magnetometer (SQUID) revealing hard and soft ferrimagnetic behavior, respectively.

1 Introduction

Green chemistry synthesis routes are currently highly attractive due to the ever growing concern about long-term sustainability [1–4]. In particular, low temperature and water-based preparation methods

Address correspondence to silvia.gross@unipd.it

are a subject of great interest within context of the synthesis of inorganic compounds.

Among inorganic materials, ferrites (described by the general chemical formulae $M^{2+}Fe_2^{3+}O_4$, $M^{2+}Fe^{4+}O_3$ or $M^{3+}Fe^{3+}O_3$, where M = metal ion) are gaining increasing attention: Thanks to their high thermal, mechanical and chemical stability [5–9], coupled with numerous functional properties (catalytic, electric, magnetic, etc.), they find applications in a large number of different fields such as magnetism and electronics [10, 11], sensor design [12], catalysis (e.g., water splitting) [13–15], and medicine [16].

In particular, spinel ferrites, the topic of the present work, find numerous applications in disparate areas of interest, ranging from electronics, to ferrofluid technologies and diagnostic medicine [17, 18], where their magnetic properties — depending on both the crystal structure of the compound and on the nature of the metal M [5, 19–21] — make them invaluable functional materials.

In the synthesis of ferrites, and in view of their potential functional applications, it is mandatory to gain a fine control over the final features of the material of choice. In this regard, it is particularly relevant to employ preparative methods allowing products with a specific composition and microstructure to be achieved. The commonly used solid state synthetic routes, besides being highly energy-consuming [22, 23], do not allow a fine control over the reaction pathways during the process. Wet chemistry routes instead appear a suitable alternative, also due to the fact that at low temperatures they yield products with smaller particle sizes.

Among wet-synthesis routes, the most commonly explored procedures for ferrite synthesis are thermal decomposition of suitable precursors [24], solvo- and hydrothermal synthesis [25, 26], reverse micelle synthesis [27, 28], polyol assisted synthesis [29], nonaqueous sol–gel [30] and coprecipitation [31]. Specifically, coprecipitation of oxalates (followed by calcination in air at high temperatures) [32] has been used to synthesize a number of spinel ferrites [33–36].

Recently we used this route, coupled with annealing at high temperatures (T = 900 °C), for the synthesis of strontium perovskite ($SrFeO_{3-\delta}$) [37] and manganese perovskite ($MnFeO_3$) [38] as well as of cobalt, nickel, zinc and magnesium spinels ($CoFe_2O_4$, $ZnFe_2O_4$, $MgFe_2O_4$, $NiFe_2O_4$) [38]. However, to the best of our knowledge, this procedure has never been combined with hydrothermal treatment in order to synthesize nanosized ferrites.

The main advantage of hydrothermal synthesis over conventional wet-chemistry methods is that it occurs under non-standard conditions and that non-classical crystallization pathways can be explored [39, 40]. By operating at relatively high autogenous pressures (generated by heating the reaction mixture within a closed vessel) several properties which are relevant for solubilization (such as ionic products, density, viscosity and dielectric constant) dramatically change, thus allowing for the dissolution of compounds which are not normally soluble under standard conditions [23, 39].

In this paper we report on the synthesis of nanosized crystalline cobalt, nickel, zinc and manganese spinel ferrites $CoFe_2O_4$, $NiFe_2O_4$, $ZnFe_2O_4$ and $MnFe_2O_4$ through a hydrothermal low-temperature route, starting from an aqueous suspension of the different metal oxalates. This method, in addition to being carried out at low temperatures, has the advantage of not requiring toxic or hard to manage reagents, and not necessitating complex purification steps. Moreover, and more importantly, the process takes place in an aqueous environment, thus making the method greener than other routes. In the literature, a study by Zhou et al. [41] has been reported concerning the synthesis of $NiFe_2O_4$ at 60 °C using a similar protocol. The reported procedure is however based on sulphate precursors, which cannot be easily eliminated during purification, unlike oxalates which decompose cleanly. Furthermore, no other compounds were obtained at such low temperatures and no data are available in the cited paper concerning sample purity and yields. Other syntheses have been reported in the literature regarding the combined use of metal oxalate precursors and hydrothermal treatment for the synthesis of titania [42], ceria [43], or hyperbranched cross-linked copper dendrites [44]. Nevertheless the synthesis of ferrites was never mentioned, nor were any of the above mentioned compounds obtained at temperatures lower than 160 °C.

In addition to this main protocol, in order to explore

the effect of pressure during the synthetic process, an alternative route (involving coprecipitation of oxalates from an aqueous solution followed by thermal decomposition under reflux conditions at 75 ℃) was adopted.

To investigate the effect of different parameters (chemical nature of the precursors, nominal molar ratio between the metals and oxalic acid, treatment time, treatment temperature) on the final features of the samples in terms of composition, purity, crystallinity degree and crystallite size, a wide range of syntheses was performed, as reported in Table 1.

Table 1 Synthesis parameters, yields and calculated average crystallite sizes for the various experiments (H- indicates hydrothermal syntheses while R- indicates reflux syntheses)

Sample	Expected formula	Nominal Fe/M/acid ratio	Treatment temperature and time	Found structure	Yield (%)	Crystallite average size (nm)
H-Co001	$CoFe_2O_4$	2/1/4.5	135 ˚C; 24 h	$CoFe_2O_4$	90	12 ± 3
H-Co007	$CoFe_2O_4$	2/1/4	135 ˚C; 24 h	$CoFe_2O_4$	99	17 ± 2
H-Co018-1	$CoFe_2O_4$	2/1/4	135 ˚C; 1 h	$CoFe_2O_4$	90	—
H-Co018-2	$CoFe_2O_4$	2/1/4	135 ˚C; 2 h	$CoFe_2O_4$	98	18 ± 3
H-Co018-4	$CoFe_2O_4$	2/1/4	135 ˚C; 4 h	$CoFe_2O_4$	98	18 ± 1
H-Co019	$CoFe_2O_4$	2/1/4	100 ˚C; 24 h	$CoFe_2O_4$	65	—
H-Co020	$CoFe_2O_4$	2/1/4	75 ˚C; 24 h	$CoFe_2O_4$	88	—
H-Mn002	$MnFe_2O_4$	2/1/4.5	135 ˚C; 24 h	$MnFe_2O_4$	100	20 ± 4
H-Mn007	$MnFe_2O_4$	2/1/4	135 ˚C; 24 h	$MnFe_2O_4$	100	49 ± 4
H-Mn012-1	$MnFe_2O_4$	2/1/4	135 ˚C; 1 h	$MnFe_2O_4$	91	25 ± 1
H-Mn012-2	$MnFe_2O_4$	2/1/4	135 ˚C; 2 h	$MnFe_2O_4$	90	33 ± 1
H-Mn012-4	$MnFe_2O_4$	2/1/4	135 ˚C; 4 h	$MnFe_2O_4$	100	24 ± 1
H-Mn013	$MnFe_2O_4$	2/1/4	100 ˚C; 24 h	$MnFe_2O_4$	91	36 ± 2
H-Mn014	$MnFe_2O_4$	2/1/4	75 ˚C; 24 h	$MnFe_2O_4$	95	35 ± 2
H-Mn015-4	$MnFe_2O_4$	2/1/4	75 ˚C; 4 h	$MnFe_2O_4$	86	35 ± 10
H-Ni001	$NiFeO_3$	1/1/3	135 ˚C; 24 h	$Ni_{1.43}Fe_{1.7}O_4$, NiO and $NiFe_2O_4$	—	20 ± 5
H-Ni002	$NiFe_2O_4$	2/1/4.5	135 ˚C; 24 h	Mixed product	—	Not calculated
H-Ni007	$NiFe_2O_4$	2/1/4	135 ˚C; 24 h	$NiFe_2O_4$	95	47 ± 2
H-Ni011-1	$NiFe_2O_4$	2/1/4	135 ˚C; 1 h	—	—	—
H-Ni011-2	$NiFe_2O_4$	2/1/4	135 ˚C; 2 h	$NiFe_2O_4$	90	10 ± 1
H-Ni011-4	$NiFe_2O_4$	2/1/4	135 ˚C; 4 h	$NiFe_2O_4$	90	34 ± 1
H-Ni012	$NiFe_2O_4$	2/1/4	100 ˚C; 24 h	$NiFe_2O_4$	65	20 ± 1
H-Ni013	$NiFe_2O_4$	2/1/4	75 ˚C; 24 h	$NiFe_2O_4$	91	8 ± 5
H-Zn001	$ZnFe_2O_4$	2/1/4	100 ˚C; 24 h	$ZnFe_2O_4$	64	5 ± 1
H-Zn002	$ZnFe_2O_4$	2/1/4	75 ˚C; 24 h	$ZnFe_2O_4$	80	4 ± 1
H-Zn003-4	$ZnFe_2O_4$	2/1/4	75 ˚C; 4 h	$ZnFe_2O_4$	64	4 ± 1
H-Zn004	$ZnFe_2O_4$	2/1/4	135 ˚C; 24 h	$ZnFe_2O_4$	92	6 ± 1
R-Zn001-24	$ZnFe_2O_4$	2/1/4	75 ˚C; 24 h	$ZnFe_2O_4$	60	4 ± 1
R-Zn002-4	$ZnFe_2O_4$	2/1/4	75 ˚C; 4 h	$ZnFe_2O_4$	57	3 ± 1
R-Zn002-2	$ZnFe_2O_4$	2/1/4	75 ˚C; 2 h	$ZnFe_2O_4$	54	4 ± 1

2 Experimental section

2.1 Chemicals

Nickel(II) chloride hexahydrate, tetraethylammonium hydroxide (20% *w*/*w* in water) (TENOH), zinc chloride, sodium hydroxide and iron(III) chloride hexahydrate were purchased from Sigma Aldrich (Milan, Italy). Oxalic acid dihydrate (99.8%), cobalt(II) chloride hexahydrate and manganese(II) acetylacetonate dihydrate were purchased from Carlo Erba (Rodano, Milan, Italy). All reagents were used without further purification.

2.2 Synthesis protocol

For the hydrothermal synthesis of a generic spinel ferrite, a suspension of metal oxalates, prepared from an aqueous mixture of metal salts and oxalic acid, was charged in an autoclave which was then heated at a set temperature for a set time span (see Table 1). The reaction scheme is shown in Scheme 1.

In detail, for a typical synthesis of a spinel MFe_2O_4 (M = Co, Mn, Ni, Zn), the defined amounts of metal M and iron precursors were dissolved in deionized water (10 mL) in a 23 mL A255AC PTFE cup (Parr Instrument Company) with constant stirring. Oxalic acid was then added as a chelating precipitant to the solution. Typically, 0.52 mmol of M precursor, 1.05 mmol of Fe precursor and 2.09 mmol of oxalic acid were used (M:Fe:acid = 1:2:4) (Table 1). A 20% *w*/*w* aqueous tetraethylammonium hydroxide solution (0.2 mL) was added as a peptizing agent [45], and the pH of the resulting solution was raised to 10 with a 10 M sodium hydroxide solution at room temperature in order to deprotonate the oxalic acid and cause the coprecipitation of metal oxalates. The resulting suspension was sealed in the PTFE cup and placed in a stainless steel 4745 General Purpose Acid-Digestion Bomb (Parr Instrument Company), heated at a set temperature for the desired time and then allowed to cool down to room temperature. The resulting solid powders were isolated by centrifugation, washed four times with deionized water and dried in an open air oven at 60 ˚C. The prepared specimens, the synthesis parameters and obtained yields are summarized in Table 1.

The synthesis of the zinc spinel $ZnFe_2O_4$ was also carried out through the alternative reflux method by dissolving $ZnCl_2$ 97% (0.073 g, 0.522 mmol), $FeCl_3{\cdot}6H_2O$ (0.287 g, 1.05 mmol) and oxalic acid dihydrate (0.296 g, 2.35 mmol) in 10 mL deionized water (within a 25 mL round-bottom flask). Following this, 0.2 mL of TENOH and 1 mL of NaOH (10 M in water) were poured into the resulting suspension under vigorous stirring. The flask was fitted with a condenser and kept for 24 h at 75 ˚C. After cooling to room temperature, the resulting

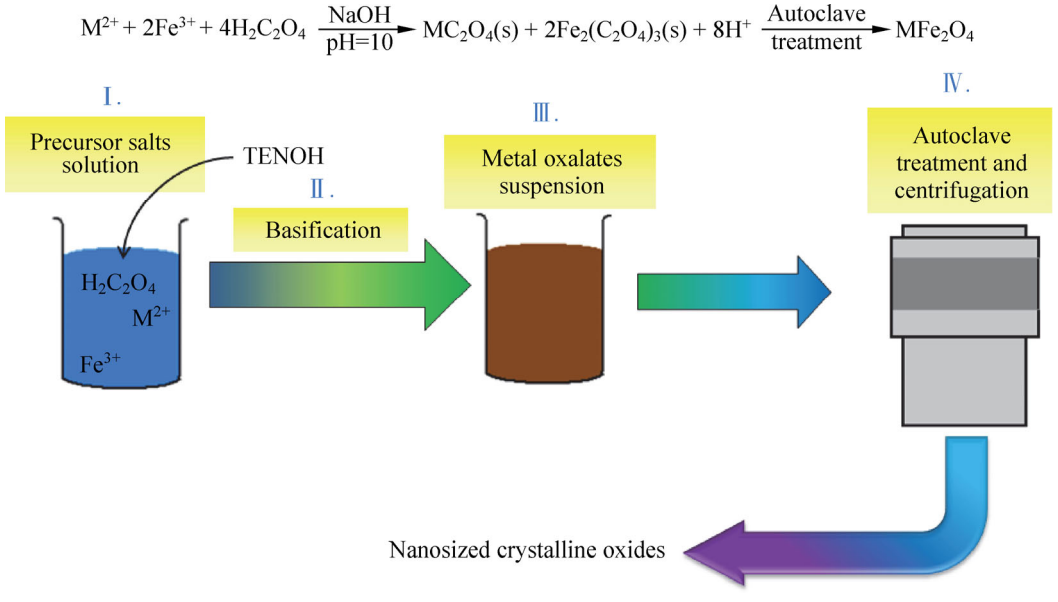

Scheme 1 Synthesis scheme.

dark red powder was isolated by centrifugation followed by washing four times with deionized water. The final product was dried in an open air oven at 60 °C. The prepared specimens, the synthesis parameters and obtained yields are summarized in Table 1.

2.3 Characterization methods

2.3.1 XPS analysis

Samples were investigated by XPS with a Φ 5600ci Perkin-Elmer spectrometer, using a standard aluminium (Al K_α) source, with an energy of 1,486.6 eV operating at 200 W. Compounds containing cobalt were investigated using a standard magnesium (Mg K_α) source with an energy of 1,253.6 eV operating at 220 W. The choice to employ a standard Mg source to analyze the cobalt samples (rather than the standard Al source employed for all other samples) was made in order to avoid the overlap of Co2p and $FeL_3M_{45}M_{45}$ peaks (both sets falling in the 775–795 eV interval with an Al source) and of the Fe2p and $CoL_2M_{23}M_{45}$ (1P) peaks (all falling in the 710–720 eV region) [46].

The X-ray source employed was located at 54.7° relative to the analyzer axis. The working pressure was < 5×10^{-8} Pa (~10^{-11} Torr). The calibration was based on the binding energy (B.E.) of the $Au4f_{7/2}$ line at 83.9 eV with respect to the Fermi level. The standard deviation for the B.E. values was 0.15 eV. The reported B.E. values were corrected for the B.E. charging effects, assigning the B.E. value of 284.6 eV to the C1s line of carbon [46–49]. Survey scans were obtained in the 0–1,350 eV range (Al source), or 0–1,200 eV range (Mg source) (pass energy 58.7 eV, 0.5 eV/step, 25 ms/step). Detailed scans (11.75–29.35 eV pass energy, 0.1 eV/step, 50–150 ms/step) were recorded for relevant regions (O1s, C1s, Fe2p, M2p) depending on the sample. The atomic composition, after a Shirley-type background subtraction [50], was evaluated using sensitivity factors supplied by Perkin-Elmer [46]. Assignment of the peaks was carried out according to literature data. The spectra were analyzed using the IGOR Pro v. 4.01 program, whereas quantitative analysis was performed using the freeware HTIS Lab XPS_AES v. 4.7 program [51]. Fitting of the peaks was performed with the XPSPEAK 4.1 freeware program [52].

2.3.2 X-ray diffraction

XRPD patterns were collected with a Bruker D8 Advance diffractometer equipped with a Göbel mirror and employing the Cu K_α radiation. The angular accuracy was 0.001° and the angular resolution was better than 0.01°. All patterns were recorded in the range 10°–80° with a 0.03° (2θ) scan step and a 7 s per step acquisition time. Patterns were analyzed through the use of the MAUD [53] program, to obtain (through Rietveld refinement) the crystallite size of the powders and data about the crystalline phases in the samples.

2.3.3 ICP–AES analysis

Metal composition was determined by using a Spectroflame Modula sequential and simultaneous ICP–AES spectrometer equipped with a capillary cross-flow nebulizer was used (Spectro Analytical, Kleve, Germany). Analytical determinations were performed using a plasma power of 1.2 kW, a radiofrequency generator of 27.12 MHz and an argon gas flow with nebulizer and a coolant set at 1, 0.5 and 14 $L \cdot min^{-1}$, respectively. The material was mineralized by treating proper amount of the samples (on the order of 50–100 mg) with 2 mL of a solution consisting of 70% HNO_3 (54 vol.%), 37% HCl (31 vol.%) and H_2O (15 vol.%). The solution obtained was diluted to 25 mL using 1% HCl.

2.3.4 Electron microscopy

Powder samples were prepared for transmission electron microscopy (TEM) observations. A small amount of each sample was suspended in ethanol using an ultrasonic bath to eliminate agglomeration. A drop of this suspension was deposited onto a carbon coated gold grid. Images of the microstructure and the relevant selected area electron diffraction (SAED) patterns were acquired using an analytical electron microscope, Philips CM12, operated at 120 keV and equipped with an energy dispersive X-ray spectroscopy (EDXS) analyzer (EDAX Falcon, with a C/U detector).

2.3.5 Magnetic measurements

The magnetic properties of the oxides were investigated by measuring the hysteresis loops at room temperature using a Cryogenic S600 superconducting quantum

device magnetometer (SQUID) that allows magnetic fields up to 50 kOe to be employed.

2.3.6 *Microanalysis*

Samples were introduced in a quartz tube which was kept at 1,020 ˚C and through which a constant flow of oxygen-enriched helium was maintained. The gases resulting from combustion passing through layers of WO_3 and metallic copper in the primary column were separated by frontal gas-chromatography through the use of a 2 m Porapak QS chromatographic column kept at 190 ˚C. The separated gas components were then analyzed with a Frisons EA 1108 analyzer. Analyses were carried out at the Department of Chemical Sciences Microanalysis Laboratory of the University of Padova.

2.3.7 *Micro-Raman spectroscopy*

Compositional and structural investigations throughout the sample were performed through micro-Raman measurements, which were carried out with a Thermo Scientific® DXR Raman Microscope using a 532 nm laser as an excitation source. Spectra were obtained with a DXR Raman Microscope (Thermo Scientific, MA, USA) equipped with an automatic stage for mapping capability as well as a 532 nm laser with a maximum laser power at sample of 10 mW. Spectra were recorded in the 3,500–50 cm^{-1} range using a full range grating with 900 lines/mm, allowing a 5 cm^{-1} FWHM resolution, and a 50× objective; an exposure time of 1.5 s averaging 40 exposures and a laser power of 1 mW were used.

3 Results and discussion

3.1 Structural, morphological and chemico-physical characterization

While, in most cases, temperatures in the range 400–1,000 ˚C are employed to obtain crystalline ferrites [54–60], in this work we observed the formation of crystals in hydrothermal conditions at temperatures as low as 75 ˚C. In fact, using the synthetic protocol described in the Experimental section, the formation of cobalt, manganese, nickel and zinc spinel oxides as a pure nanosized phase at temperatures as low as 75 ˚C and in as short reaction times as 2 h was evidenced. The resulting compounds were obtained in high yields, crystallinity degree and purity. This is, to the best of our knowledge, an unprecedented and very exciting result. Moreover, by employing a sealed glass vial as a reactor, it was evidenced that ferrite formation took place rapidly at 135 ˚C, as the brown precursor suspensions rapidly changed into a dark precipitate. The process however, requires a high pressure environment, since simple thermal treatment of the precursors turned out to be insufficient even for the removal of crystallization water. Furthermore, the role of the aqueous medium was also highlighted, since the temperature observed is much lower than temperatures reported in literature for the decomposition of metal oxalates [61–65] which, in solid state, takes place at over 200 ˚C.

In order to evaluate the influence of a closed system on the synthetic procedure in general and on the crystallinity of the final product in particular, attempts were carried out by heating the Zn and Fe oxalate suspension at 75 ˚C for 24, 4 and 2 h under reflux conditions (Table 1). In all cases, the crystalline spinel phase was successfully obtained. Samples synthesized with this method however had, compared to their counterparts prepared through the hydrothermal route, a lower yield and displayed a higher carbon and hydrogen content (0.81% and 1.22% respectively, compared to 0.24% and 0.37% for sample H-Zn002, see Table 2), showing that a larger amount of organic precursors remained adsorbed on the final powder.

The structure of the hydrothermally synthesized ferrites (Fig. 1) and the ferrites prepared through reflux synthesis (Fig. S1 in the Electronic Supplementary Material (ESM)) was thoroughly investigated by XRPD allowing also an estimation of the average crystallite size (Table 1). From the crystallinity point of view, no relevant differences were observed between compounds synthesized by the two different routes, as

Table 2 Microanalysis results for different spinel samples

Sample	Content	Found C (%)	Found H (%)
H-Co007	$CoFe_2O_4$	0.25	0.35
H-Mn007	$MnFe_2O_4$	0.13	0.20
H-Ni007	$NiFe_2O_4$	0.70	0.43
H-Zn002	$ZnFe_2O_4$	0.24	0.37
R-Zn002-4	$ZnFe_2O_4$	0.81	1.22

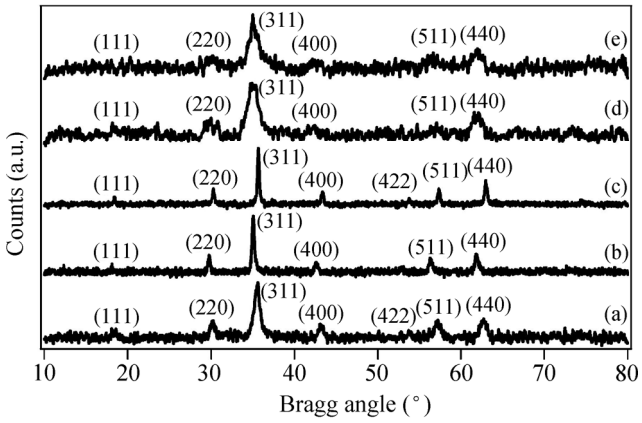

Figure 1 XRPD patterns of (a) H-Co007, (b) H-Mn007, (c) H-Ni007, (d) H-Zn001 and (e) H-Zn004.

evidenced by the comparison between XRPD patterns relative to $ZnFe_2O_4$ synthesized through the two protocols and reported in Fig. S2 (in the ESM). XRPD patterns were fitted basing the initial calculations on information available in the literature [66–71] in order to perform Rietveld refinement. Patterns were interpolated using the Le Bail algorithm [72] together with the least weighed squares method. In the case of the cobalt spinel, the Maximum Entropy Electron Maps (MEEM) algorithm was employed in addition to the above mentioned methods. The resulting plot was used as a starting point to estimate the atomic position within the unit cell (Fig. S3 in the ESM).

In general, the characteristics of the obtained compounds did not significantly change with temperature, treatment time and synthesis protocol, showing that in all cases the reaction occurs rapidly and does not require intense heat. Crystallite size was however shown to be slightly influenced by the temperature parameter as, at lower temperature, marginally smaller crystallites were obtained, an aspect particularly evident in the Zn based materials. These observations are consistent with a nucleation process prevailing over crystal growth at lower temperatures. Manganese spinel is an exception to this trend, as the crystallite size did not display significant changes with temperature (Fig. S4 in the ESM). Cobalt samples treated at lower temperatures (75–100 °C) yielded patterns with reflections which were too broad to estimate the crystallite size: Although the reflections were visible, the high background caused by X-ray fluorescence, which is considerable in samples containing cobalt and iron [73], effectively masked a large part of them, making an accurate estimate impossible.

The picture emerging from the XRPD analyses was substantially confirmed by TEM observations. The Zn ferrites (Figs. 2(d)–2(f)), all processed at comparatively low temperatures, display (both in the case of hydrothermal and reflux synthesis) a homogeneous microstructure, featuring crystallites with an average size below 10 nm, in good agreement with the results obtained from Rietveld refinement. The corresponding SAED patterns (insets in the relevant TEM micrographs and Figs. S5–S10 in the ESM) confirm this finding, as a uniform distribution of the diffracted intensities is observed, indicating that a large number of randomly oriented crystallites is present in the imaged field of view. Coherently, a coarser microstructure is displayed by materials processed at higher temperatures, e.g., 135 °C (Figs. 2(a)–2(c)). In agreement with the XRPD data, crystallites are, in this case, of 20–50 nm in size, with a broader dimension range. Actually, sample H-Ni007 has a properly bimodal crystallite size distribution and at least two markedly

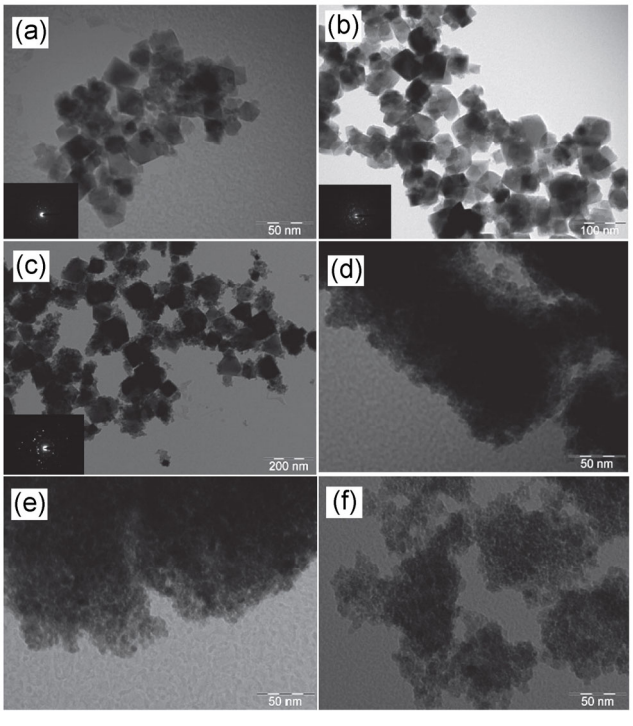

Figure 2 TEM micrographs (with SAED patterns) of (a) H-Co007, (b) H-Mn007, (c) H-Ni007, (d) H-Zn001, (e) R-Zn002-2 and (f) R-Zn002-4 (for enlargements of SAED patterns, see Figs. S5–S10 in the ESM).

different grain morphologies, the larger one corresponding to well crystallized particles, with platelike aspect; the other one with rounded, significantly smaller domains.

Micro-Raman spectroscopy was employed to gain insight into the vibrational energy states within the compounds, as well as to assess the compositional uniformity throughout the powders [74]. Measurements were carried out on samples yielded spectra (Fig. 3) which display all the peaks characteristic of cobalt [75, 76], manganese [77], nickel [78, 79] and zinc [77, 80] spinel ferrites, with all main documented Raman-active phonon modes present [81, 82]. Given that all three compounds show a very similar crystal structure (cubic cell, $Fd\bar{3}m$ space group, Z equal to 8) [66–68, 70], they display the same phonon modes ($A_{1g} + E_g + 3T_{2g}$) [75–77] though, due to peak overlap, not all modes are readily distinguishable in the figure. The same overlap renders it extremely complex to distinguish site distribution within the spinel lattice directly from the spectra [75]. The fact however that Raman spectroscopic data is indicative of a spinel structure, further confirms the results gathered through XRD and XPS. Moreover, the micro-Raman spectroscopy allowed several spectra to be collected at different points on each sample, all of which yielded similar results, confirming the uniformity of the compound composition and structure throughout the samples.

Microanalyses (Table 2) were conducted in order to estimate the amount of organic residue from the precursor compounds adsorbed on the synthesized

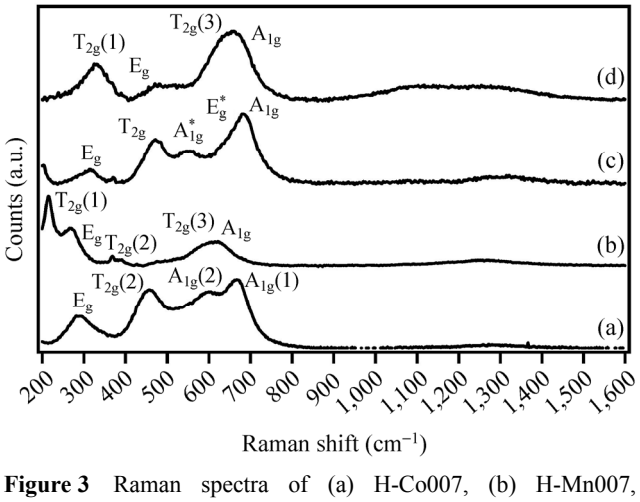

Figure 3 Raman spectra of (a) H-Co007, (b) H-Mn007, (c) H-Ni007 and (d) H-Zn002.

oxides. The investigations show that only a very small amount of organic residue from the synthetic process is present in the final product, thus proving its effectiveness in obtaining pure oxide compounds.

Despite this, the nominal atomic ratio between the metal precursors and oxalic acid was found to have a significant impact on the final products: Syntheses carried out with a higher oxalic acid nominal ratio (M:Fe:acid = 1:2:4.5 rather than 1:2:4) in many cases displayed unidentified secondary phases. The nominal metal precursor atomic ratio also appears to be a critical factor in determining whether single or multiple phases are obtained. For example, nickel ferrite sample H-Ni001 was prepared with a Fe:Ni atomic ratio of 1, rather than the stoichiometric 2 and consequently yielded a mixture of phases consisting of the nickel spinel $NiFe_2O_4$, NiO and the spinel species $Ni_{1.43}Fe_{1.7}O_4$. It should be noted that the two impurity phases were not initially distinguishable through XRPD (Fig. S11 in the ESM). This can be ascribed to two different factors: Firstly, both spinel compounds ($NiFe_2O_4$ and the non stoichiometric spinel $Ni_{1.43}Fe_{1.7}O_4$) (Table S1 in the ESM) have a cubic $Fd\bar{3}m$ cell with very similar parameters; secondly, reflections relative to NiO (Fig. S11 in the ESM) can be masked by $NiFe_2O_4$ reflections (provided the nickel oxide is only present in small quantities and therefore relevant reflections have a very low intensity). For these reasons the presence of secondary phases was only inferred by combining the diffraction data with ICP–AES results (Table 3), enabling an accurate determination of metal content in the samples: Only the presence of multiple phases would account for the detected Fe:Ni ratio (1:1).

In this regard, ICP–AES analyses (Table 3) were carried out on samples to obtain an unambiguous determination of the bulk Fe:M molar ratios. In the case of H-Co001 and H-Mn002 (Fe/M = 2.013 and 2.055 respectively), data in agreement with expected stoichiometry (i.e., Fe/M = 2) were obtained. In the case of sample H-Ni001, a much lower Fe:Ni atomic ratio was detected (Fe/M = 1.027) which was consistent with nominal Fe:Ni precursor ratios, but not with the desired stoichiometry ($NiFe_2O_4$). This was attributed to the presence of the above mentioned secondary NiO and $Ni_{1.43}Fe_{1.7}O_4$ phases.

Surface composition (Table 3) obtained through

Table 3 Surface composition (XPS—carbon not reported) and Fe:M (XPS and ICP) atomic ratios measured in selected samples

Sample	Compound	M (%) (atomic)	Fe (%) (atomic)	O (%) (atomic)	O:(Fe+M) atomic ratio (from XPS)	Fe:M atomic ratio (from XPS)	Fe:M atomic ratio (from ICP–AES)
H-Co001	$CoFe_2O_4$	1.8	3.7	25.3	4.6	2.1	2.01
H-Co007	$CoFe_2O_4$	4.2	8.3	26.7	2.1	2.0	—
H-Co020	$CoFe_2O_4$	1.9	3.9	34.0	5.9	2.1	—
H-Mn002	$MnFe_2O_4$	4.9	8.7	20.8	1.4	1.8	2.05
H-Mn007	$MnFe_2O_4$	2.7	5.0	18.7	2.5	1.9	—
H-Mn014	$MnFe_2O_4$	4.9	9.8	40.7	2.8	2.0	—
H-Ni001	$Ni_{1.43}Fe_{1.7}O_4$ + $NiFe_2O_4$	6.4	4.4	23.0	2.1	0.7	1.03
H-Ni007	$NiFe_2O_4$	3.5	7.1	24.5	2.5	2.0	2.09
H-Ni013	$NiFe_2O_4$	4.5	8.9	45.8	3.4	2.0	—
H-Zn002	$ZnFe_2O_4$	2.7	7.2	29.4	3.3	2.7	—
R-Zn002-4	$ZnFe_2O_4$	5.9	15.8	49.9	2.5	2.7	—

XPS analysis, and in particular surface Fe:M atomic ratios, were in agreement with the surface literature concentrations for cobalt [83, 84], manganese [83, 84], zinc [83, 85] and nickel spinel ferrites [83]. This finding proves the purity of the samples (except for some small amounts of sodium impurities, as can be seen in the XPS surveys) and is consistent throughout the samples regardless of the treatment temperature involved. This confirms the data gathered through XRPD indicating that the compounds were obtained as pure crystalline single phases. It should be also noted that surface oxygen concentration, though included for the sake of completion, was not compared to the data in literature as it is highly dependent on sample synthesis and preparation prior to XPS analysis.

High-resolution XPS analyses were performed on the O1s, C1s, Fe2p and second metal (Co2p, Mn2p, Ni2p, Zn2p) regions for all samples. The C1s peak at 284.6 eV (adventitious carbon) was used as reference in order to correct the spectra for surface charge [46, 48]. The XPS spectra (Fig. 4) showed binding energy (B.E.) values (Table 4) in agreement with the

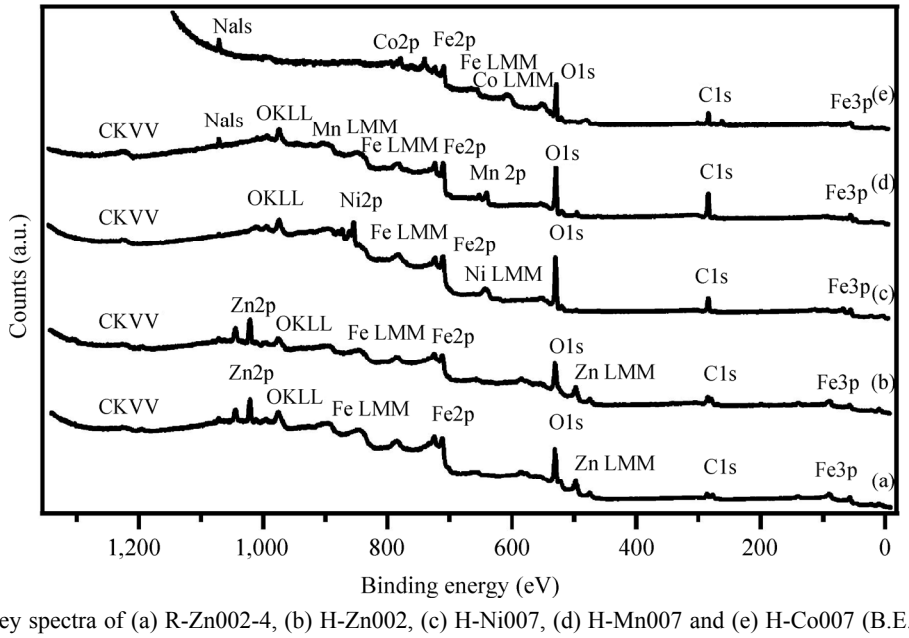

Figure 4 XPS survey spectra of (a) R-Zn002-4, (b) H-Zn002, (c) H-Ni007, (d) H-Mn007 and (e) H-Co007 (B.E. values corrected for charging effects).

Table 4 Surface binding energies of studied elements in the different prepared compounds (corrected for charging effects)

Sample	Element	Peak	B.E. (eV)
H-Co007	O	1s	529.4
	Fe	$2p_{3/2}$ and $2p_{1/2}$	710.6 and 723.7
	Co	$2p_{3/2}$ and $2p_{1/2}$	779.4 and 794.8
H-Mn007	O	1s	529.3
	Fe	$2p_{3/2}$ and $2p_{1/2}$	710.0 and 723.1
	Mn	$2p_{3/2}$ and $2p_{1/2}$	641.0 and 652.8
H-Ni007	O	1s	529.7
	Fe	$2p_{3/2}$ and $2p_{1/2}$	709.2 and 722.3
	Ni	$2p_{3/2}$ and $2p_{1/2}$	854.9 and 872.6
H-Zn002	O	1s	529.5
	Fe	$2p_{3/2}$ and $2p_{1/2}$	710.7 and 723.8
	Zn	$2p_{3/2}$ and $2p_{1/2}$	1020.6 and 1043.6

literature data for $ZnFe_2O_4$ [86], $CoFe_2O_4$ [84], $MnFe_2O_4$ [84, 87], $NiFe_2O_4$ [88, 89], confirming that pure spinel oxides had been formed.

In all the samples, the Fe2p peak (Fig. S12 in the ESM) displayed a satellite ($Fe2p_{3/2}$) peak at a B.E. value 8 eV higher than the main peak, which is consistent with compounds containing the Fe^{III} oxidation state, as expected [46, 83, 84, 87, 88], while none of the samples (Fig. S12 in the ESM) displayed a satellite ($Fe2p_{3/2}$) peak at 6 eV higher than the main peak (which would be indicative of the presence of Fe^{II}), thus showing that all detectable surface iron is present as Fe^{III} [88]. This is consistent with the data reported in the literature [90, 91] and, despite the inversion of the spinel structures, confirms that even in tetrahedral sites, iron maintains an oxidation state of Fe^{III}. The region is practically identical in all three samples; this is in agreement with the fact that all three compounds present a similar MFe_2O_4 structure with similar chemical environments.

Concerning the Mn ferrite, the Mn2p peak (Fig. S13 in the ESM) displays broad peaks which are indicative of the simultaneous presence of multiple chemical environments. Due to multiplet splitting typical of Mn2p, interpretation is complex [92–94]. Peak positions and broadness however are consistent with the presence of Mn^{II} and Mn^{IV} in an oxide environment [87, 95]. The co-presence of surface manganese in these two oxidation states is consistent with reported data on $MnFe_2O_4$ [87, 96].

As far as the nickel spinel is concerned, the Ni2p (Fig. S14 in the ESM) is devoid of the satellite peak at 1.2 eV (which, if present together with a slightly lower binding energy of the main peak, would indicate the presence of surface NiO [88, 89]). Peak positions and spectral shape are consistent with the presence of Ni^{II} on the surface [90, 91]. The broad shape of the peaks, as well as the presence of asymmetries indicative of shoulder peaks suggests that a certain quantity of nickel hydroxide might be present on the surface [97] (possibly due to surface energies and reaction with air humidity).

In the case of the zinc ferrites, the two peaks in the Zn2p region of sample H-Zn002 (Fig. S15 in the ESM) are symmetrical, sharp and well defined, showing that all surface zinc is present in the same chemical environment. Identical results were also obtained for sample R-Zn002-4 (Fig. S16 in the ESM). Both these data and the B.E. values displayed by the peaks are in agreement with data in the literature [86, 98, 99] for $ZnFe_2O_4$ and ZnO (if we consider the spinel system as equivalent to a combination of ZnO and Fe_2O_3). The detection of a single chemical environment is also consistent with the zinc ferrite being a normal spinel [60], since it implies all zinc atoms occupy the same type of site (i.e., tetrahedral).

3.2 Functional characterization: Magnetic behavior

As mentioned in the introduction, most spinels display ferrimagnetic properties and are widely used as soft magnetic materials [100–102]. The cobalt spinel $CoFe_2O_4$ however is an exception to this rule [100, 102], behaving as a hard magnetic material.

To assess the magnetic behavior of two different types of synthesized ferrite (i.e., the cobalt and manganese spinels) the compounds were investigated by measurement of their hysteresis loops (Figs. 5 and 6).

The coercive fields of the cobalt and manganese ferrite are 780 Oe and 60 Oe, respectively. Moreover, while the magnetization of the manganese ferrite saturates at low magnetic fields, the two branches of the hysteresis loop for the cobalt ferrite close at high fields (6 kOe) and larger magnetic fields are required to saturate the magnetization. Both the coercive field values and the shape of the hysteresis loops confirm

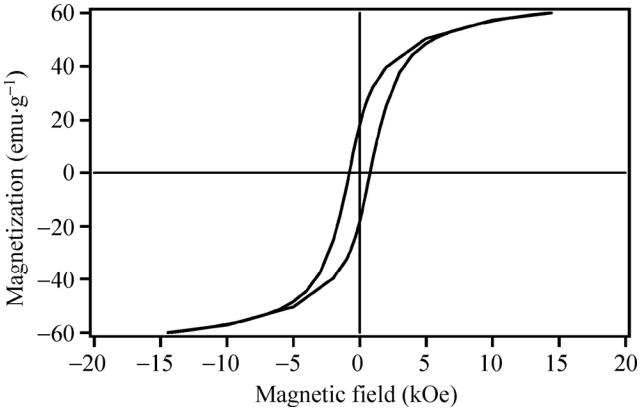

Figure 5 Room temperature hysteresis loop for H-Co007.

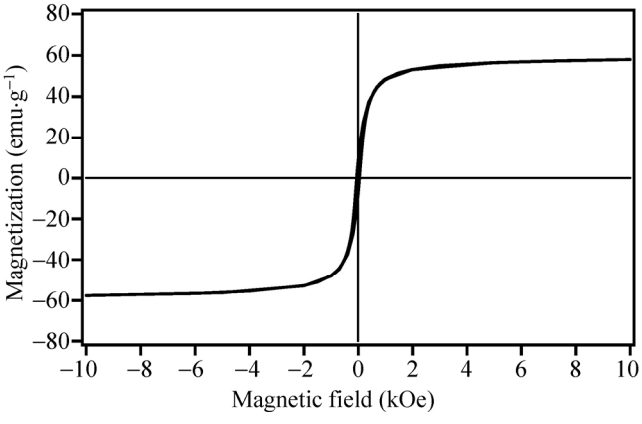

Figure 6 Room temperature hysteresis loop for H-Mn008.

the soft and hard magnetic properties of the manganese and cobalt ferrites, respectively [102, 103].

The values of the magnetization of the Mn and Co ferrites at the maximum magnetic field of 60 kOe are 61.0 emu/g and 67.7 emu/g respectively. Considering the magnetization values of bulk Mn and Co ferrites (80 emu/g and 75 emu/g respectively [104]), the magnetization of the synthesized oxides is 25% and 10% smaller, respectively. The smaller magnetizations could be due to spin disorder at the particle surface or to the chemical disorder characteristic of the nanocrystalline nature of these oxides [105–109].

The results show that the manganese ferrite is a much softer magnetic material than its cobalt analogue; this is consistent with typical spinel ferrite behavior.

3.3 Crystallization under hydrothermal conditions: Mechanistic hypothesis

This study was devoted to the low temperature synthesis under hydrothermal conditions of crystalline ferrites and to assess the effect of the different experimental parameters (chemical nature of the precursors, nominal molar ratio between the metals and oxalic acid, treatment time, treatment temperature) on the crystallization pathways. Though, as mentioned in the Introduction, hydrothermal syntheses of these compounds have already been previously reported for cobalt [110, 111], zinc [112, 113], nickel [41, 114] and manganese [113, 114], the method explored in this work is particularly notable due to the high quality of the resulting compounds and the very low temperatures involved. To account for these very surprising results, the particular conditions presented by hydrothermal synthesis and the changes occurring in the chemical and physical properties of the solvent should be considered. It has to be noted that, in order for crystallization to take place in an aqueous medium, precipitation must occur slowly from a supersaturated solution [115]. During hydrothermal synthesis this can take place due to the non-standard conditions which the system is subjected to, allowing for the solubilization of normally insoluble compounds [23, 39]. The most widely acknowledged theory regarding formation of ceramic oxide particles through hydrothermal synthesis [39, 116, 117] involves a two-step mechanism. In the first phase (*in situ* transformation), the precursor ions are dissolved in the reaction mixture: Given the conditions under which the reaction takes place, tiny quantities of the target oxide are able to form (as solutes) in the liquid phase. Due to the low solubility, even at high pressure and temperature, of the final compound, the second phase (precipitation and growth) takes place. In this phase, nucleation centers are formed throughout the system around which crystal growth can occur. Considering the small size of the crystallites prepared by this method, it can be assumed that these nucleation centers form quite rapidly compared to the growth process. This difference in kinetics results in the formation of a large number of small crystalline nanostructures, as opposed to a series of larger particles. It can be hypothesized that a similar multi-stage process occurs during the syntheses described above: Under the non-standard reaction conditions, part of the coprecipitated metal oxalates are solubilized and form the target spinel ferrites

which then nucleate and undergo particle growth resulting in a nanocrystalline precipitate. The possible decomposition of oxalate ions to CO_2 would cause an increase in reaction pressure, which would further facilitate the solubilization and successive precipitation events.

4 Conclusions

Spinel mixed ferrites $CoFe_2O_4$, $MnFe_2O_4$, $NiFe_2O_4$ and $ZnFe_2O_4$ have been obtained for the first time through a fast, easily reproducible, high yield (63%–100%) and very low temperature wet-synthesis route, combining coprecipitation of oxalates and hydrothermal treatment.

The chosen methodology allowed for the preparation of pure nanocrystalline ceramic oxides at temperatures as low as 75 ˚C in an aqueous environment, and neither required special costly equipment, nor produced relevant amounts of polluting waste. The speed at which the reaction occurs suggests that both nucleation and growth processes have very fast kinetics. Although it was possible to reproduce the syntheses under reflux conditions (i.e., in an open system), the resulting products displayed lower purity and were obtained with lower yields compared to hydrothermal syntheses. This can be likely attributed to the lower pressure involved (which is possibly further enhanced during hydrothermal synthesis by decomposition of the oxalate precursors to CO_2). This low temperature decomposition is made possible by the aqueous environment. Characterizations, through X-ray diffraction and TEM, have shown these particles to be nanosized with crystallites in the 10–50 nm range (for Co, Mn and Ni ferrites) and 5 nm range (for the zinc spinels). ICP–AES investigations confirmed that this route affords a very good stoichiometric control over the products. The ferrimagnetic behavior of the prepared manganese and cobalt spinels was evidenced by SQUID measurements. Investigation of the mechanism of the synthetic route revealed the process to be sensitive to the stoichiometric ratio between the precipitating agent and the metal salts, as an excess of oxalic acid lead to the formation of secondary phases. On the other hand, treatment temperature in the 75–135 ˚C range had a limited effect on the crystallite size of the final oxides.

Acknowledgements

The Italian National Research Council (CNR), the Ph.D. School in Molecular Sciences of the University of Padova and PRIN-2010–BNZ3F2 Project DESCARTES (Development of Energy-targeted Self-assembled supramolecular systems: a Convergent Approach through Resonant information Transfer between Experiments and Simulations) of the Italian Ministry of the University and Research are acknowledged for financial support. The MIUR is acknowledged for financial support to the FIRB project "FIRB2012 INCYPIT (INnovative Ceramic and hYbrid materials for Proton conducting fuel cells at Intermediate Temperature): design, characterization and device assembly" and "FIRB2010 RINAME (Integrated Network for Nano Medicine)". Regione Lombardia and Consorzio INSTM for financial support to project MAGNANO (Tailoring MAGnetic NANOparticles physical properties for advanced clinical application), of the call 2013. Dr. Keti Vezzù (University of Padova) is gratefully acknowledged for the ICP–AES analyses. Dr. Roberta Saini (University of Padova) is thanked for TGA–DSC measurements. Dr. César de Julià Fernàndez and Dr. Massimiliano Rocchia are acknowledged for the helpful discussion of the data on magnetism and Raman spectroscopy, respectively. Thermo Scientific Rodano (MI) Italy is thanked for the micro-Raman measurements.

Electronic Supplementary Material: Supplementary material (XRPD patterns, MEEM plots, SAED micrographs, XRPD pattern comparison, crystal cell parameters and XPS spectra) is available in the online version of this article at http://dx.doi.org/10.1007/s12274-014-0466-3

References

[1] Dahl, J. A.; Maddux, B. L. S.; Hutchison, J. E. Toward greener nanosynthesis. *Chem. Rev.* **2007**, *107*, 2228–2269.

[2] Song, C. Fuel processing for low-temperature and high-temperature fuel cells. Challenges, and opportunities for sustainable development in the twenty-first century. *Catal. Today* **2002** *77*, 17–49.

[3] Trost, B. M. On inventing reactions for atom economy. *Acc. Chem. Res.* **2002**, *35*, 695–705.

[4] Herrmann, J. M.; Duchamp, C.; Karkmaz, M.; Hoai, B. T.; Lachheb, H.; Puzenat, E.; Guillard, C. Environmental green chemistry as defined by photocatalysis. *J. Hazard. Mater.* **2007**, *146*, 624–629.

[5] Greenwood, N. N.; Earnshaw, A. *Chemistry of the Elements, 2nd Ed.*; Pergamon Press: India, 1998.

[6] Cotton, F. A.; Wilkinson, G. *Advanced Inorganic Chemistry, 5th Ed.*; John Wiley & Sons: New York, 1988.

[7] Holleman, A. F.; Wieberg, E. *Lehrbuch der Anorganischen Chemie, 101st Ed.*; Walter de Gruyter: New York, 1995.

[8] Kung, H. H. *Transition Metal Oxides: Surface Chemistry and Catalysis*. Elsevier: Amsterdam, 1989.

[9] Rao, C. N. R.; Raveau, B. *Transition Metal Oxides: Structure, Properties and Synthesis of Ceramic Oxides*. Wiley VCH: Weinheim, 2009.

[10] de Muro, I. G.; Insausti, M.; Lezama, L.; Rojo, T. Effects of the synthesis conditions on the magnetic and electrical properties of the $BaFeO_{3-x}$ oxide: Ametamagnetic behaviour. *J. Solid State Chem.* **2005**, *178*, 1712–1719.

[11] Deng, Y.; Zhou, J. X.; Wu, D.; Du, Y. L.; Zhang, M. S.; Wang, D. H.; Yu, H. Q.; Tang, S. L.; Du, Y. W. Three-dimensional phases-connectivity and strong magnetoelectric response of self-assembled feather-like $CoFe_2O_4$–$BaTiO_3$ nanostructures. *Chem. Phys. Lett.* **2010**, *496*, 301–305.

[12] Rezlescu, N.; Doroftei, C.; Popa, P. D. Humidity-sensitive electrical resistivity of $MgFe_2O_4$ and $Mg_{0.9}Sn_{0.1}Fe_2O_4$ porous ceramics. *Rom. J. Phys.* **2007**, *52*, 353–360.

[13] Florea, M.; Alifanti, M.; Parvulescu, V. I.; Mihaila-Tarabasanu, D.; Diamandescu, L.; Feder, M.; Negrila, C.; Frunza, L. Total oxidation of toluene on ferrite-type catalysts. *Catal. Today* **2009**, *141*, 361–366.

[14] Scheffe, J. R.; Li, J.; Weimer, A. W. A spinel ferrite/hercynite water-splitting redox cycle. *Int. J. Hydrogen Energ.* **2010,** *35*, 3333–3340.

[15] Menini, L.; Pereira, M. C.; Parreira, L. A.; Fabris, J. D.; Gusevskaya, E. V. Cobalt- and manganese-substituted ferrites as efficient single-site heterogeneous catalysts for aerobic oxidation of monoterpenic alkenes under solvent-free conditions. *J. Catal.* **2008**, *254*, 355–364.

[16] Latham, A. H.; Williams, M. E. Controlling transport and chemical functionality of magnetic nanoparticles. *Acc. Chem. Res.* **2008**, *41*, 411–420.

[17] Colombo, M.; Carregal-Romero, S.; Casula, M. F.; Gutierrez, L.; Morales, M. P.; Boehm, I. B.; Heverhagen, J. T.; Prosperi, D.; Parak, W. J. Biological applications of magnetic nanoparticles. *Chem. Soc. Rev.* **2012**, *41*, 4306–4334.

[18] Gijs, M. A. M.; Lacharme, F.; Lehmann, U. Microfluidic applications of magnetic particles for biological analysis and catalysis. *Chem. Rev.* **2010**, *110*, 1518–1563.

[19] Nordhei, C.; Ramstad, A. L.; Nicholson, D. G. Nanophase cobalt, nickel and zinc ferrites: Synchrotron XAS study on the crystallite size dependence of metal distribution. *Phys. Chem. Chem. Phys.* **2008**, *10*, 1053–1066.

[20] Costa, A. C. F. M.; Tortella, E.; Morelli, M. R.; Kiminami, R. H. G. A. Synthesis, microstructure and magnetic properties of Ni–Zn ferrites. *J. Magn. Magn. Mater.* **2003**, *256*, 174–182.

[21] Thummer, K. P.; Chantbar, M. C.; Modi, K. B.; Baldha, G. J.; Joshi, H. H. Localized canted spin behaviour in $Zn_xMg_{1.5-x}Mn_{0.5}FeO_4$ spinel ferrite system. *J. Magn. Magn. Mater.* **2004**, *280*, 23–30.

[22] Niederberger, M.; Pinna, N. *Metal Oxide Nanoparticles in Organic Solvents—Synthesis, Formation, Assembly and Applications*; Springer: New York, 2009.

[23] Schubert, U.; Hüsing, N. *Synthesis of Inorganic Materials, 2nd Ed.*; Wiley-VCH: Weinheim, 2005.

[24] Bao, N. Z.; Shen, L. M.; Wang, Y. H.; Padhan, P.; Gupta, A. A facile thermolysis route to ferrite nanocrystals. *J. Am. Chem. Soc.* **2007**, *129*, 12374–12375.

[25] Modeshia, D. R.; Walton, R. I. Solvothermal synthesis of perovskites and pyrochlores: Crystallization of functional oxides under mild conditions. *Chem. Soc. Rev.* **2010**, *39*, 4303–4325.

[26] Pinna, N.; Grancharov, S.; Beato, P.; Bonville, P.; Antonietti, M.; Niederberger, M. Magnetite nanocrystals: Nonaqueous synthesis, characterization, and solubility. *Chem. Mater.* **2005**, *17*, 3044–3049.

[27] Grasset, F.; Labhsetwar, N.; Li, D.; Park, D. C.; Saito, N.; Haneda, H.; Cador, O.; Roisnel, T.; Mornet, S.; Duguet, E. et al. Synthesis and magnetic characterization of zinc ferrite nanoparticles with different environments: Powder, colloidal solution, and zinc ferrite–silica core–shell nanoparticles. *Langmuir* **2002**, *18*, 8209–8216.

[28] Sun, S.; Zeng, H.; Robinson, D. B.; Raoux, S.; Rice, P. M.; Wang, S. X.; Li, G. Monodisperse MFe_2O_4 (M = Fe, Co, Mn) nanoparticles. *J. Am. Chem. Soc.* **2004**, *126*, 273–279.

[29] Baldi, G.; Bonacchi, D.; Lorenzi, G.; Innocenti, C.; Sangregorio, C. Cobalt ferrite nanoparticles: The control of the particle size and surface state and their effects on magnetic properties. *J. Magn. Magn. Mater.* **2007**, *311*, 10–16.

[30] Niederberger, M. Nonaqueous sol–gel routes to metal oxide nanoparticles. *Acc. Chem. Res.* **2007**, *40*, 793–800.

[31] Wu, J. H.; Ko, S. P.; Liu, H. L.; Kim, S.; Ju, J. S.; Kim, K. Y. Sub 5 nm magnetite nanoparticles: Synthesis, microstructure, and magnetic properties. *Mater. Lett.* **2007**, *61*, 3124–3129.

[32] Rigby, E.; Kehr, W.; Meldrum, C. Preparation of coprecipitated NiZn ferrite. *IEEE T. Magn.* **1984**, *20*, 1506–1508.

[33] Kanade, S. A.; Puri, V. Properties of thick film $Ni_{0.6}Co_{0.4}Fe_yMn_{2-y}O_4$: ($0 \leqslant y \leqslant 0.5$) NTC ceramic. *J. Alloys. Compd.* **2009**, *475*, 352–355.

[34] Gabal, M. A.; Al, A. Y. M. Effect of diamagnetic substitution on the structural, magnetic and electrical properties of $NiFe_2O_4$. *Mater. Chem. Phys.* **2009**, *115*, 578–584.

[35] Toberer, E. S.; Joshi, A.; Seshadri, R. Template-free routes to macroporous monoliths of nickel and iron oxides: Toward porous metals and conformally coated pore walls. *Chem. Mater.* **2005,** *17*, 2142–2147.

[36] Wang, M.; Ai, Z.; Zhang, L. Generalized preparation of porous nanocrystalline $ZnFe_2O_4$ superstructures from zinc ferrioxalate precursor and its superparamagnetic property. *J. Phys. Chem. C* **2008**, *112*, 13163–13170.

[37] Diodati, S.; Nodari, L.; Natile, M. M.; Russo, U.; Tondello, E.; Lutterotti, L.; Gross, S. Highly crystalline strontium ferrites $SrFeO_{3-\delta}$: An easy and effective wet-chemistry synthesis. *Dalton Trans.* **2012**, *41*, 5517–5525.

[38] Diodati, S.; Nodari, L.; Natile, M. M.; Caneschi, A.; de Julián Fernández, C.; Hoffmann, C.; Kaskel, S.; Lieb, A.; Di Noto, V.; Mascotto, S. et al. Coprecipitation of oxalates: An easy and reproducible wet-chemistry synthesis route for transition metal ferrites. *Eur. J. Inorg. Chem.* **2014**, 875–887.

[39] Byrappa, K.; Yoshimura, M. *Handbook of Hydrothermal Technology*; Noyes Publications: Park Ridge, New Jersey, U.S.A, 2001.

[40] Lobachev, A. N. *Crystallization Processes Under Hydrothermal Conditions, 1st Ed.*; Consultants Bureau: New York, 1973.

[41] Zhou, J.; Ma, J. F.; Sun, C.; Xie, L. J.; Zhao, Z. Q.; Tian, H.; Wang, Y. G.; Tao, J. T.; Zhu, X. Y. Low-temperature synthesis of $NiFe_2O_4$ by a hydrothermal method. *J. Am. Ceram. Soc.* **2005**, *88*, 3535–3537.

[42] Truong, Q. D.; Le, T. H.; Liu, J.-Y.; Chung, C.-C.; Ling, Y.-C. Synthesis of TiO_2 nanoparticles using novel titanium oxalate complex towards visible light-driven photocatalytic reduction of CO_2 to CH_3OH. *Appl. Catal. A—Gen.* **2012**, *437–438*, 28–35.

[43] Zhang, G. J.; Shen, Z. R.; Liu, M.; Guo, C. H.; Sun, P. C.; Yuan, Z. Y.; Li, B. H.; Ding, D. T.; Chen, T. H. Synthesis and characterization of mesoporous ceria with hierarchical nanoarchitecture controlled by amino acids. *J. Phys. Chem. B* **2006**, *110*, 25782–25790.

[44] Truong, Q. D.; Kakihana, M. Hydrothermal growth of cross-linked hyperbranched copper dendrites using copper oxalate complex. *J. Crystal Growth* **2012**, *348*, 60–64.

[45] Yang, J.; Mei, S.; Ferreira, J. M. F. Hydrothermal synthesis of nanosized titania powders: Influence of tetraalkyl ammonium hydroxides on particle characteristics. *J. Am. Ceram. Soc.* **2001**, *84*, 1696–1702.

[46] Moulder, J. F.; Stickle, W. F.; Sobol, P. E.; Bomben, K. D. *Handbook of X-ray Photoelectron Spectroscopy—A Reference Book of Standard Spectra for Identification and Interpretation of XPS Data*; Perkin-Elmer Corp.: Eden Prarie, Minnesota, 1992.

[47] NIST XPS Database—Version 3.5. http://srdata.nist.gov/xps/.

[48] Briggs, D.; Seah, M. P. *Practical Surface Analysis: Volume 1—Auger and X-ray Photoelectron Spectroscopy, 2nd Ed.*; John Wiley & Sons: New York, 1990.

[49] Wang, Z. G.; Zu, X. T.; Zhu, S.; Wang, L. M. Green luminescence originates from surface defects in ZnO nanoparticles. *Phys. E.* **2006**, *35*, 199–202.

[50] Shirley, D. A. High-resolution X-ray photoemission spectrum of the valence bands of gold. *Phys. Rev. B* **1972**, *5*, 4709–4713.

[51] High Tech International Services Snc *XPS_AES Program v. 4.7*; www.htis.it, 2006.

[52] Kwok, R. H. W. *XPSPEAK, 4.1*; University of Hong Kong: Hong Kong, 1994.

[53] Lutterotti, L. *MAUD Program*; Università degli Studi di Trento: Trento, 1998.

[54] Aono, H.; Hirazawa, H.; Naohara, T.; Maehara, T. Surface study of fine $MgFe_2O_4$ ferrite powder prepared by chemical methods. *Appl. Surf. Sci.* **2008**, *254*, 2319–2324.

[55] Bayoumi, W. Structural and electrical properties of zinc-substituted cobalt ferrite. *J. Mater. Sci.* **2007**, *42*, 8254–8261.

[56] Kakihana, M.; Yoshimura, M. Synthesis and characteristics of complex multicomponent oxides prepared by polymer complex method. *Bull. Chem. Soc. Jpn.* **1999**, *72*, 1427–1443.

[57] Lessing, P. A. Mixed-cation oxide powders via polymeric precursors. *Am. Ceram. Soc. Bull.* **1989**, *68*, 1002–1007.

[58] Segal, D. Chemical synthesis of ceramic materials. *J. Mater. Chem.* **1997**, *7*, 1297–1305.

[59] Jiang, Q.-H.; Nan, C.-W.; Shen, Z.-J. Synthesis and properties of multiferroic La-modified $BiFeO_3$ ceramics. *J. Am. Ceram. Soc.* **2006**, *89*, 2123–2127.

[60] Haetge, J.; Suchomski, C.; Brezesinski, T. Ordered mesoporous MFe_2O_4 (M = Co, Cu, Mg, Ni, Zn) thin films with nanocrystalline walls, uniform 16 nm diameter pores and high thermal stability: Template-directed synthesis and characterization of redox active trevorite. *Inorg. Chem.* **2010**, *49*, 11619–11626.

[61] Broadbent, D.; Dollimore, D.; Dollimore, J. The thermal decomposition of oxalates. Part V. The thermal decomposition of nickel oxalate dihydrate. *J. Chem. Soc. A* **1966**, 278–281.

[62] Broadbent, D.; Dollimore, D.; Dollimore, J. The thermal decomposition of oxalates. Part IX. The thermal decomposition of the oxalate complexes of iron. *J. Chem. Soc. A* **1967**, 451–454.

[63] Dollimore, D.; Griffiths, D. L.; Nicholson, D. The thermal decomposition of oxalates. Part II. Thermogravimetric analysis of various oxalates in air and in nitrogen. *J. Chem. Soc.* **1963**, 2617–2623.

[64] Dollimore, D.; Nicholson, D. The thermal decomposition of oxalates. Part VI. The decomposition and surface properties of ferric oxalate. *J. Chem. Soc. A* **1966**, 281–284.

[65] Dollimore, D.; Nicholson, D. The thermal decomposition of oxalates. Part I. The variation of surface area with the temperature of treatment in air. *J. Chem. Soc.* **1962**, 960–965.

[66] Gull, S. F.; Daniell, G. J. Image reconstruction from incomplete and noisy data. *Nature* **1978**, *272*, 686–690.

[67] Wychoff, R. W. G. *Structure of Crystals*; The Chemical Catalogue Company Inc.: New York, 1931.

[68] Passerini, L. Ricerche sugli spinelli. II. I composti: $CuAl_2O_4$; $MgAl_2O_4$; $MgFe_2O_4$; $ZnAl_2O_4$; $ZnCr_2O_4$; $ZnFe_2O_4$; $MnFe_2O_4$. *Gazz. Chim. Ital.* **1930**, *60*, 389–399.

[69] Montoro, V. Miscibilità tra gli ossidi di ferro e di manganese. *Gazz. Chim. Ital.* **1938**, *68*, 728–733.

[70] Kremnović, A.; Antić, B.; Vučinić-Vasić, M.; Colomban, P.; Jovalekić, C.; Bibić, N.; Kahlenberg, V.; Leoni, M. Temperature-induced structure and microstructure evolution of nanostructured $Ni_{0.9}Zn_{0.1}O$. *J. Appl. Cryst.* **2010**, *43*, 699–709.

[71] Crystallography Open Database. http://www.crystallography.net/.

[72] Le Bail, A. In *Proceedings of the International Conference on Accuracy in powder Diffraction ll*. NIST, Gaithersburg, 1992, pp142–153.

[73] Ceccone, G.; Marmorato, P.; Ponti, J.; Rossi, F.; Kaulich, B.; Gianocelli, A.; Pascolo, L.; Salome, M.; Kiskinova, M. *Synchrotron radiation X-ray fluorescence mapping of cobalt ferrite nanoparticles in Balb/3T3 fibroblast cells*. Pacifichem 2010—International Chemical Congress of Pacific Basin Societies, Honolulu, U.S.A., 2010.

[74] Schrader, B. *Infrared and Raman Spectroscopy: Methods and Applications, 1st Ed.*; VCH: Weinheim, Germany, 1995.

[75] Ayyappan, S.; Mahadevan, S.; Chandramohan, P.; Srinivasan, M. P.; Philip, J.; Raj, B. Influence of Co^{2+} ion concentration on the size, magnetic properties, and purity of $CoFe_2O_4$ spinel ferrite nanoparticles. *J. Phys. Chem. C* **2010**, *114*, 6334–6341.

[76] Chandramohan, P.; Srinivasan, M. P.; Velmurugan, S.; Narasimhan, S. V. Cation distribution and particle size effect on Raman spectrum of $CoFe_2O_4$. *J. Solid State Chem.* **2011**, *184*, 89–96.

[77] Varshney, D.; Verma, K.; Kumar, A. Structural and vibrational properties of $Zn_xMn_{1-x}Fe_2O_4$ (x = 0.0, 0.25, 0.50, 0.75, 1.0) mixed ferrites. *Mater. Chem. Phys.* **2011**, *131*, 413–419.

[78] Ahlawat, A.; Sathe, V. G.; Reddy, V. R.; Gupta, A. Mossbauer, Raman and X-ray diffraction studies of superparamagnetic $NiFe_2O_4$ nanoparticles prepared by sol–gel auto-combustion method. *J. Magn. Magn. Mater.* **2011**, *323*, 2049–2054.

[79] Lazarević, Z. Ž.; Jovalekić, Č.; Milutinović, A.; Romcević, M. J.; Romcević, N. Ž. Preparation and characterization of nano ferrites. *Acta Phys. Pol. A* **2012**, *121*, 682–686.

[80] Wang, Z. W.; Schiferl, D.; Zhao, Y. S.; O'Neill, H. S. C. High pressure Raman spectroscopy of spinel-type ferrite $ZnFe_2O_4$. *J. Phys. Chem. Solids* **2003**, *64*, 2517–2523.

[81] Nongjai, R.; Khan, S.; Asokan, K.; Ahmed, H.; Khan, I. Magnetic and electrical properties of In doped cobalt ferrite nanoparticles. *J. Appl. Phys.* **2012**, *112*, 084321.

[82] Yamashita, O.; Ikeda, T. Effect of polishing stress on Raman spectra of the Mn–Zn ferrite. *J. Appl. Phys.* **2004**, *95*, 1743–1748.

[83] Lee, H.; Jung, J. C.; Kim, H.; Chung, Y.-M.; Kim, T. J.; Lee, S. J.; Oh, S.-H.; Kim, Y. S.; Song, I. K. Effect of divalent metal component (Me^{II}) on the catalytic performance of $Me^{II}Fe_2O_4$ catalysts in the oxidative dehydrogenation of n-butene to 1,3-butadiene. *Catal. Lett.* **2008**, *124*, 364–368.

[84] Zhang, S. X.; Niu, H. Y.; Cai, Y. Q.; Zhao, X. L.; Shi, Y. L. Arsenite and arsenate adsorption on coprecipitated bimetal oxide magnetic nanomaterials: $MnFe_2O_4$ and $CoFe_2O_4$. *Chem. Eng. J.* **2010**, *158*, 599–607.

[85] Domenichini, B.; Pataut, G.; Bourgeois, S. Stabilization of polar solid oxide surfaces: Competition between adsorption and reconstruction. *Surf. Interface Anal.* **2002**, *34*, 540–544.

[86] Bera, S.; Prince, A. A. M.; Velmurugan, S.; Raghavan, P. S.; Gopalan, R.; Panneerselvam, G.; Narasimhan, S. V. Formation of zinc ferrite by solid-state reaction and its characterization by XRD and XPS. *J. Mater. Sci.* **2001**, *36*, 5379–5384.

[87] Herranz, T.; Rojas, S.; Ojeda, M.; Pérez-Alonso, F. J.; Terreros, P.; Pirota, K.; Fierro, J. L. G. Synthesis, structural features, and reactivity of Fe–Mn mixed oxides prepared by microemulsion. *Chem. Mater.* **2006**, *18*, 2364–2375.

[88] Mittal, V. K.; Bera, S.; Nithya, R.; Srinivasan, M. P.; Velmurugan, S.; Narasimhan, S. V. Solid state synthesis of Mg–Ni ferrite and characterization by XRD and XPS. *J. Nucl. Mater.* **2004**, *335*, 302–310.

[89] Mittal, V. K.; Chandramohan, P.; Bera, S.; Srinivasan, M. P.; Velmurugan, S.; Narasimhan, S. V. Cation distribution in $Ni_xMg_{1-x}Fe_2O_4$ studied by XPS and Mössbauer spectroscopy. *Solid State Commun.* **2006**, *137*, 6–10.

[90] Baruwati, B.; Rana, R. K.; Manorama, S. V. Further insights in the conductivity behavior of nanocrystalline $NiFe_2O_4$. *J. Appl. Phys.* **2007**, *101*, 014302.

[91] Nawale, A. B.; Kanhe, N. S.; Patil, K. R.; Bhoraskar, S. V.; Mathe, V. L.; Das, A. K. Magnetic properties of thermal plasma synthesized nanocrystalline nickel ferrite ($NiFe_2O_4$). *J. Alloys. Compd.* **2011**, *509*, 4404–4413.

[92] Glisenti, A.; Natile, M. M.; Galenda, A. $PrMnO_3$ prepared by the citrate gel method, studied by XPS. *Surf Sci. Spec.* **2009**, *16*, 67–74.

[93] Murray, J. W.; Dillard, J. G.; Giovanoli, R.; Moers, H.; Stumm, W. Oxidation of manganese (II): Initial mineralogy, oxidation state and ageing. *Geochim. Cosmochim. Ac.* **1985**, *49*, 463–470.

[94] Gupta, R. P.; Sen, S. K. Calculation of multiplet structure of core p-vacancy levels. *Phys. Rev. B* **1974**, *10*, 71–77.

[95] Kim, K. J.; Lee, H. J.; Park, J. Y. Cationic behavior and the related magnetic and magnetotransport properties of manganese ferrite thin films. *J. Magn. Magn. Mater.* **2009**, *321*, 3706–3711.

[96] Hu, J.; Lo, I. M. C.; Chen, G. H. Fast removal and recovery of Cr(VI) using surface-modified jacobsite ($MnFe_2O_4$) nanoparticles. *Langmuir* **2005**, *21*, 11173–11179.

[97] Natile, M. M.; Glisenti, A. Surface reactivity of NiO: Interaction with methanol. *Chem. Mater.* **2002**, *14*, 4895–4903.

[98] Bardhan, A.; Ghosh, C. K.; Mitra, M. K.; Das, G. C.; Mukherjee, S.; Chattopadhyay, K. K. Low temperature synthesis of zinc ferrite nanoparticles. *Solid State Sci.* **2010**, *12*, 839–844.

[99] Tahir, A. A.; Wijayantha, K. G. U. Photoelectrochemical water splitting at nanostructured $ZnFe_2O_4$ electrodes. *J. Photoch. Photobio. A* **2010**, *216*, 119–125.

[100] Dionne, G. F. *Magnetic Oxides, 1st Ed.*; Springer: London, 2009.

[101] Tilley, R.J. D. *Understanding Solids—The Science of Materials*; J. Wiley & Sons: Chichester, West Sussex, England, 2004.

[102] Coey, J. M. D. *Magnetism and Magnetic Materials, 1st Ed.*; Cambridge University Press: New York, 2010.

[103] Özgür, Ü.; Alivov, Y.; Morkoç, H. Microwave ferrites, part 1: Fundamental properties. *J. Mater. Sci.: Mater. Electron.* **2009**, *20*, 789–834.

[104] Lu, H. M.; Zheng, W. T.; Jiang, Q. Saturation magnetization of ferromagnetic and ferrimagnetic nanocrystals at room temperature. *J. Phys. D: Appl. Phys.* **2007**, *40*, 320–325.

[105] Linderoth, S.; Hendriksen, P. V.; Bødker, F.; Wells, S.; Davies, K.; Charles, S. W.; Mørup, S. On spin-canting in maghemite particles. *J. Appl. Phys.* **1994**, *75*, 6583–6585.

[106] Batlle, X.; Labarta, A. Finite-size effects in fine particles: Magnetic and transport properties. *J. Phys. D: Appl. Phys.* **2002**, *35*, R15–R42.

[107] Peddis, D.; Yaacoub, N.; Ferretti, M.; Martinelli, A.; Piccaluga, G.; Musinu, A.; Cannas, C.; Navarra, G.; Greneche, J. M.; Fiorani, D. Cationic distribution and spin canting in $CoFe_2O_4$ nanoparticles. *J. Phys.: Condens. Matter* **2011**, *23*, 426004.

[108] Kim, B. H.; Lee, N.; Kim, H.; An, K.; Park, Y. I.; Choi, Y.; Shin, K.; Lee, Y.; Kwon, S. G.; Na, H. B. et al. Large-scale synthesis of uniform and extremely small-sized iron oxide nanoparticles for high-resolution T_1 magnetic resonance imaging contrast agents. *J. Am. Chem. Soc.* **2011**, *133*, 12624–12631.

[109] Sun, Q.-C.; Birkel, C. S.; Cao, J. B.; Tremel, W.; Musfeldt, J. L. Spectroscopic signature of the superparamagnetic transition and surface spin disorder in $CoFe_2O_4$ nanoparticles. *ACS Nano* **2012**, *6*, 4876–4883.

[110] Zhang, Y.; Liu, Y.; Fei, C. L.; Yang, Z.; Lu, Z. H.; Xiong, R.; Yin, D.; Shi, J. The temperature dependence of magnetic properties for cobalt ferrite nanoparticles by the hydrothermal method. *J. Appl. Phys.* **2010**, *108*, 084312.

[111] Zhao, L. J.; Zhang, H. J.; Xing, Y.; Song, S. Y.; Yu, S. Y.; Shi, W. D.; Guo, X. M.; Yang, J. H.; Lei, Y. Q.; Cao, F. Studies on the magnetism of cobalt ferrite nanocrystals synthesized by hydrothermal method. *J. Solid State Chem.* **2008**, *181*, 245–252.

[112] Fan, G. L.; Gu, Z. J.; Yang, L.; Li, F. Nanocrystalline zinc ferrite photocatalysts formed using the colloid mill and hydrothermal technique. *Chem. Eng. J.* **2009**, *155*, 534–541.

[113] Chen, L. Y.; Shen, Y. M.; Bai, J. F. Large-scale synthesis of uniform spinel ferrite nanoparticles from hydrothermal decomposition of trinuclear heterometallic oxo-centered acetate clusters. *Mater. Lett.* **2009**, *63*, 1099–1101.

[114] Ren, G.-H.; Yu, Z.-S. Synthesis of monodisperse Fe_3O_4 and $MnFe_2O_4$ nanospheres by using a solvothermal reduction method. *Solid State Phenom.* **2012**, *181–182*, 393–396.

[115] Holden, A.; Singer, P. *Crystals and Crystal Growing*; Anchor Books Doubleday & Company Inc.: Garden City, New York, 1971.

[116] Chen, X. L.; Fan, H. Q.; Liu, L. J. Synthesis and crystallization behavior of lead titanate from oxide precursors by a hydrothermal route. *J. Cryst. Growth* **2005**, *284*, 434–439.

[117] MacLaren, I.; Ponton, C. B. A TEM and HREM study of particle formation during barium titanate synthesis in aqueous solution. *J. Eur. Ceram. Soc.* **2000**, *20*, 1267–1275.